Hydroxylation of Apollo 17 Soil Sample 78421 by Solar Wind Protons

J. L. McLain[1], M. J. Loeffler[1,2,3], W. M. Farrell[1], C. I. Honniball[1], J. W. Keller[1], and R. Hudson[1]

[1]NASA Goddard Space Flight Center, Greenbelt, MD 20771
[2]Department of Astronomy and Planetary Science, Northern Arizona University, Flagstaff, AZ, 86011
[3]Center for Materials Interfaces in Research and Applications, Northern Arizona University, Flagstaff, AZ, 86011

Corresponding author: Jason L. McLain (jason.l.mclain@nasa.gov)

Key Points:

- Laboratory measurements show solar wind energy protons produce hydroxyls in Apollo 17 lunar sample 78421
- Diffuse reflectance infrared spectra of 78421 show the OH band near 3 μm increases in wavelength and broadens due to space weathering
- Newly formed hydroxyls diffuse during heating to 400 K, and up to 25% are lost

Abstract

Hydroxylation by solar wind protons has been simulated in our laboratory on Apollo 17 lunar sample 78421, a very mature regolith sample that is rich with agglutinates (68%). The goal of this study was to determine the rate of hydroxyl formation and their thermal stability by monitoring changes in the SiOH (hydroxyl) stretching band near 3 μm using diffuse reflectance FTIR spectroscopy (DRIFTS). A 2 keV H_2^+ ion beam was used to simulate proton implantation on 78421 and on a crushed fused silica sample. We find that the OH band does not change unless the samples have been annealed in vacuum prior to irradiation. Qualitatively, the OH bands for the fused silica and 78421 are very different. The OH band for fused silica is centered at 2.74 μm and is relatively sharp ranging from 2.67 - 3.1 μm at full-width-at-half-maximum (FWHM), while the OH band for 78421 is centered at 3.0 μm and ranges from 2.74 - 3.37 μm at FWHM. The increase in wavelength and broadened nature of the OH band in 78421 may be associated with the OH's proximity to surface defects and/or lattice vacancies. The lack of the H_2O bending mode at 6.1 μm indicates that any adsorbed terrestrial H_2O is below our detection limit, and therefore the H_2O stretching mode at 2.9 μm is not significantly contributing to the broad 3 μm OH band and implies that proton implantation by itself does not lead to water formation. To simulate the maximum dayside temperature on the lunar surface, the lunar sample was heated after proton irradiation. The proton induced OH concentration was reduced by as much as 25% after heating to 400 K (127 °C).

Plain Language Summary

We performed laboratory experiments to mimic solar wind protons implanting into lunar soils. We measured changes in the OH absorption band near 3 microns using infrared spectroscopy to determine the rate of hydroxyl formation and their thermal stability after proton irradiation. The lunar sample designated 78421, was collected during Apollo 17's manned mission to the Moon. The 78421 sample is composed mostly of clumps of small grains that were exposed to the harsh environment of space. For these experiments, we used a crushed fused silica powder as a control sample for the experiment. Our spectral data shows that the absorption band for OH is much broader for the Apollo sample than for the fused silica control. We did not observe a corresponding bending mode for H_2O at 6.1 μm, which indicates that water is not produced during proton implantation and that the OH stretch near 3 μm is not from adsorbed water. After heating our proton irradiated Apollo soil to 400 K (127 °C), the Moon's midday surface temperature, a reduction of up to 25% of the initial OH band area was observed indicating that hydroxyls (or hydrogen) can diffuse in or out of the lunar grains during the day.

1. Introduction

Solar wind induced hydroxylation on the Moon and other airless bodies is critically important to understand how space weathering produces and distributes potential hydrogen-bearing resources such as water. Our understanding of these hydrogen-bearing resources was significantly advanced in 2009 and 2010 when hydroxyls in the mid-latitude and cool terminator regolith was observed via infrared spectroscopy [*Clark*, 2009; *Pieters et al.*, 2009; *Sunshine et al.*, 2009], and when water-ice within permanently shadowed polar craters was confirmed [*Colaprete et al.*, 2010]. The few percent depth of this hydroxyl 2.8 μm absorption band is consistent with concentrations of OH/H_2O at 10-1000 ppm. It was suggested that solar wind proton implantation was a possible source for the OH absorption feature [*McCord et al.*, 2011; *Pieters et al.*, 2009]. In this case, solar wind protons at 1 keV would implant into the oxygen-bearing regolith, and some fraction of the implanted hydrogen would form OH via interactions with oxygen residing in the lunar regolith.

This process of creating OH in oxygen bearing minerals was described before these 2009/2010 discoveries [*Zeller et al.*, 1966]. *Fink et al.* [1995] found that proton-irradiated silica samples could retain hydrogen via hindered diffusion: the migrating H atoms form metastable OH bonds with irradiation-damaged sites in the silica crystal lattice. *L V Starukhina* [2006] presented a model of solar wind proton implantation and subsequent H diffusion in the crystal lattice, where the H was considered mobile and the O atoms remained bound to a parent atom (Si, Fe, etc.). Like Fink et al. suggest, the H atoms would diffuse by migrating from O to O, with the H being temporarily bound to O atoms to form the metastable O-H bonds. The dwell time of the metastable O-H bonds can be long since the trapping potential is relatively large for the irradiation damaged silica.

Several ion implantation laboratory studies followed the initial OH discovery 2009 reports. *Burke et al.* [2011] irradiated anorthite and ilmenite samples with 1 and 100 keV protons but found no evidence for the formation of OH. *Ichimura et al.* [2012] irradiated Apollo 16 and 17 samples with a 2.2 keV H_2^+ beam, and using IR reflectance analysis they directly detected the formation of an OH absorption feature between 2.7 and 3.7 μm. *Schaible and Baragiola* [2014]

irradiated amorphous silica and olivine with 2-10 keV protons, and detected an OH band near 3 μm.

Since the 2009 discovery papers, there have been several attempts to model the H implantation and diffusion process (e.g., [*Farrell et al.*, 2017; *Farrell et al.*, 2015b]. *Tucker et al.* [2019] used a global Monte Carlo code to examine solar wind implantation and subsequent H diffusion using interatomic diffusion parameters from Fink et al. (1995). Fink et al. also included the release of implanted hydrogen into the exosphere as molecular hydrogen via recombinative desorption ($H + H \rightarrow H_2$.) The work thus connected the solar wind implantation process to the observed H_2 exosphere, with the outgassed exospheric H_2 component being the primary end product of the implantation process. [*Farrell et al.*, 2015a] found that Fink-like diffusion of implanted solar wind hydrogen is consistent with the reported mid-latitude diurnal loss of hydrogen in warm regions [*Li and Milliken*, 2017], and the exospheric density of the resulting H_2 outgassing was found to also be consistent with the LAMP-measured H_2 density of 2000-9000/cm^3 [*Hurley et al.*, 2017; *Stern et al.*, 2013]. A more H-retentive surface having higher H diffusion activation energy compared to Fink et al. [1995] was found to form more OH than observed and therefore creates a lower H_2 exospheric density than observed. Fink et al. also found that while most of the implanted H diffuses out of the surface as H_2, some small fraction is retained at mid- and high-latitudes due to diffusion paths that have relatively high activation energy, and thus are not recombining during the lunar diurnal thermal cycling in the regolith. These long-lived implanted H atoms were thought to effectively 'heal' the surface, filling in the highest binding potential sites created by radiation and impact damage to the crystal lattice.

Jones et al. [2018] have suggested that solar wind proton implantation also creates interstitial OH that migrates as a molecule in the lattice (as opposed to H migrating from parent-bound O to O as modeled by Starukhina (2006)). Jones et al. also simulated the possibility that some fraction of these OH molecules form surface-escaping water molecules via recombinative desorption: $OH + H \rightarrow H_2O$. While this process may be viable, the conversion rate of the solar wind protons into exospheric water has to be low (less than 1 part in 10000) to remain consistent with the LADEE NMS exospheric water detection limit of < 1 cm^{-3} [*Benna et al.*, 2019].

Upon looking at the laboratory experiments that have shown ion-induced formation of the near 3 μm absorption features, we noticed that the shape of the OH absorption band appears to vary significantly. In particular, the feature shown in Ichimura et al. (2012) was significantly broader than in Schaible and Baragiola (2014). Whether the broader absorption band was characteristic of lunar samples or due to something else is unclear, but it is critically important for proper interpretation of lunar remote sensing data. Thus, in this study we compare the effects of proton implantation on two different silicate samples. Specifically, we irradiated crushed fused silica and lunar sample 78421 with 2 keV H_2^+ and studied the formation of the OH infrared band. Samples were prepared, irradiated, and analyzed under the same conditions, enabling us to directly compare the influence of initial mineralogy differences on the 2.8 μm OH absorption feature, as well as to further validate the difference in the H trapping potential between unweathered silica and mature space-weathered lunar samples.

2. Materials and Methods

2.1 Sample Preparation

Crushed fused silica was chosen as a control sample due to its oxygen-rich nature and prevalence of experimental studies in the literature involving the silica hydroxyls (silanols). The fused silica was from Reade®, purity 99.99%, and was sieved to <150 μm. The focus of this paper was lunar sample 78241.38. Lunar sample 78421 was retrieved from a trench dug at Station 8 during Apollo 17. It contains an abundance of agglutinates (68%), has a maturity index of Is/FeO = 92, and an average grain size of 51 μm [*Graf*, 1993; *Morris*, 1978]. The silica powder or lunar sample was weighed and placed into a small alumina boat. The sample and alumina boat were placed inside a 38 mm quartz tube, inserted into a Carbolite® tube furnace and evacuated with a turbo pump down to pressures of ~1×10^{-7} Torr. While under vacuum, the sample was heated to 900 °C at a rate of 8 °C/min while maintaining a pressure ~1×10^{-6} Torr. The sample was held at 900 °C for 4 hours, and then allowed to cool to room temperature in vacuum. The sample then was placed into an aluminum washer and pressed into a pellet with 6 MPa of pressure. This allowed us to mount the pellet vertically in the irradiation chamber. After the samples were secured in the washer, reflectance spectra were obtained. Next, the sample pellets were inserted into the UHV irradiation chamber, which was pumped down to ~10^{-9} Torr. The sample holder can accommodate up to two pellets enabling successive irradiations of the silica and 78421 sample pellets.

2.2 Experimental Methods

Proton irradiations were performed in a UHV chamber at NASA Goddard Space Flight Center's Radiation Effects Facility. The proton source was a lower energy 0.5 - 5 keV OCI Vacuum Microengineering IG70 gas fed ion gun using UHP grade H_2 gas. For these experiments, a 2 keV H_2^+ ion beam current was used to irradiate the samples. [*Wieser et al.*, 2002] have shown that H_2^+ with similar energies to those used in our study dissociates upon impact with a solid target, producing protons that are the same average energy (1 keV) as those found in the solar wind. Ion scattering time-of-flight studies with incident H_2^+ energies from 300 - 1500 eV showed that no H_2^+ or H_2 neutrals were detected, and indicated that the incident H_2^+ dissociates upon impact with a solid MgO target [*Wieser et al.*, 2002]. The resulting momentum transfer of the 2 keV H_2^+ beam gives two H atoms with ~1 keV each, where the scattered charge state is mainly energetic H^0, with ~20% converted to H^+ and H^-. Furthermore, from the Wieser experiments, the charge state of the scattering fraction does not depend on the primary proton charge, e.g., H^- or H^+ will result in the same scattered charge state. The implication of the scattering results indicates that our bombarding H_2^+ beam energy is at the peak of the average solar wind proton energy [*Wieser et al.*, 2009]. During each experiment, the ion flux was typically $5.5 \pm 1.5 \times 10^{14}$ 1 keV protons/cm^{2}s, which was determined by a Faraday cup positioned at the top of the sample mount. The Faraday cup shield was biased at -20 V to prevent low-energy secondary electron escape.

After irradiation, the samples were removed from the chamber and mounted inside a Pike Technologies EasiDiff® reflectance accessory located in the sample compartment of a Nicolet iS50 Fourier Transform Infrared (FTIR) spectrometer. The transfer took ~10 min, and the spectrometer was continuously purged with dry air and housed the diffuse reflectance accessory. The IR spectra were collected using a liquid nitrogen cooled MCT-A detector from 8000 to 650 cm^{-1} or 1.25 to 15.3 μm at a resolution of 4 cm^{-1}. The resulting diffuse reflectance (DRIFTS)

spectrum (R/R_0) was obtained by dividing the reflected intensity of the irradiated samples (R) by the reflected intensity of the samples prior to irradiation (R_0) for silica. For clarity, R_1 refers to the reflected intensity of sample 78421 prior to irradiation. To ensure we were only looking at the processed sample, the IR beam's aperture size was set to focus onto the sample to a diameter of ~2 mm, much smaller than the ion beam diameter of ~1 cm.

To assess the thermal stability of the products in our irradiated sample, we fabricated a new sample slide mount out of aluminum to hold the samples while heating from room temperature up to 400 K using a 100 W cartridge heater. A Type K thermocouple attached to the aluminum slide mount was used to monitor the temperature. On our experimental setup, there was no active cooling and the samples and sample holder warmed slightly during irradiation which in turn affects the diffusion (reemission) rate. In the future, we will determine the proton induced hydroxylation concentration *in situ*, and its dependence on surface temperature as described by the *Farrell et al.* [2017] hydroxylation model.

3. Results

3.1 Fused Silica Control and Spectral Background

The proton-induced hydroxylation experiments show that 2 keV H_2^+ can react to produce a thermally stable OH as shown by the presence and increasing strength of the bands at 2.74 μm and 3.0 μm in Figures 1 and 2 for fused silica and 78421, respectively. We point out that we did not see any spectral change near 3.0 μm in our experiments if the samples were not annealed prior to H_2^+ irradiation. However, we did not examine the dependence of annealing temperature prior to irradiation on band shape or depth. The null result indicates that the samples already contained copious amounts of surface OHs (data not shown here), and proton exchange reactions dominate hydroxylation as shown by [*Ichimura et al.*, 2012] with H_2^+/D_2^+ irradiation experiments. For our experiments, a change in the OH band occurs only when most of the surface and interstitial hydroxyls are removed. The dehydroxylation/rehydroxylation process for silica has been described previously by Zhuravlev [2000]. According to Zhuravlev, above ~900 °C, rehydroxylation with excess water becomes a slow, strongly activated process [*Zhuravlev*, 2000]. Interestingly, our baked fused silica sample was hydrophobic and drops of water only "bead up" on the surface. Furthermore, after our baked silica sample was boiled in water for 5 minutes, and then dried for ~30 min, the IR spectrum still did not show an increase of the OH or H_2O bands. This is definitive proof that long times (days) and/or very warm/wet conditions are required to affect the 3 μm band after intense baking. In addition, we also show in Figure 3 that the H_2O bending mode is absent, which indicates adsorbed telluric water does not significantly contribute to the OH bands and that proton irradiation alone does not form trapped water.

Crushed fused silica was used as a control sample for the proton-induced hydroxylation experiments. Figure 1 shows IR spectra of the baked fused silica as a function of proton irradiation fluence, where the reference, R_0, is the reflected intensity of the sample prior to irradiation. The top spectrum is the ratio of the reflected intensity of the backside of the sample after irradiation to R_0. The lack of any absorption feature in the spectrum, other than the residual water vapor in the beam path (the structure between 2.5 to 2.8 μm) confirms that no significant amount of adsorbed water accumulates on the sample surface during the experiment. In contrast, irradiation clearly produces an OH feature. For instance, after an initial fluence of $7.8 \pm 1.8 \times 10^{18}$ 1 keV H^+/cm^2, the SiOH band centered at 2.74 μm is evident. The SiOH band has an almost vertical slope at the lower wavelength, indicative of a fused silica with surface hydroxyls.

Besides the OH band there are also other features evident between 3.3 to 3.6 μm, which are due to CH stretches likely from organics (adventitious carbon) adsorbed onto the baked fused silica. These CH band peaks are pointing upward in both lower two spectra, which indicate that they have decreased because of irradiation. This decrease is expected as the protons sputter the surface layers of the fused silica sample where the organics are adsorbed. Note that the top spectrum in Figure 1 "No Irradiation" does not have this feature because it was not bombarded with the proton beam.

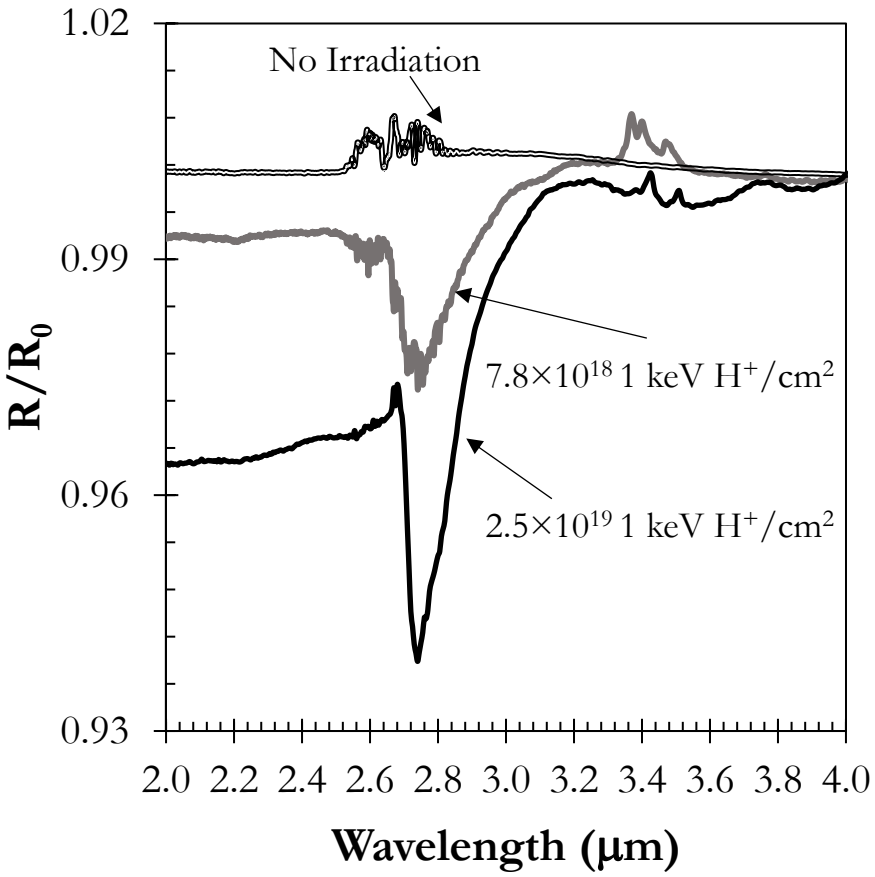

Figure 1. DRIFTS spectra of fused silica before and after proton irradiation. The spectra from top to bottom correspond to the unirradiated fused silica (ratioed to the back of sample) and after fluences of 0.78 and 2.5×10^{19} 1 keV H^+/cm^2.

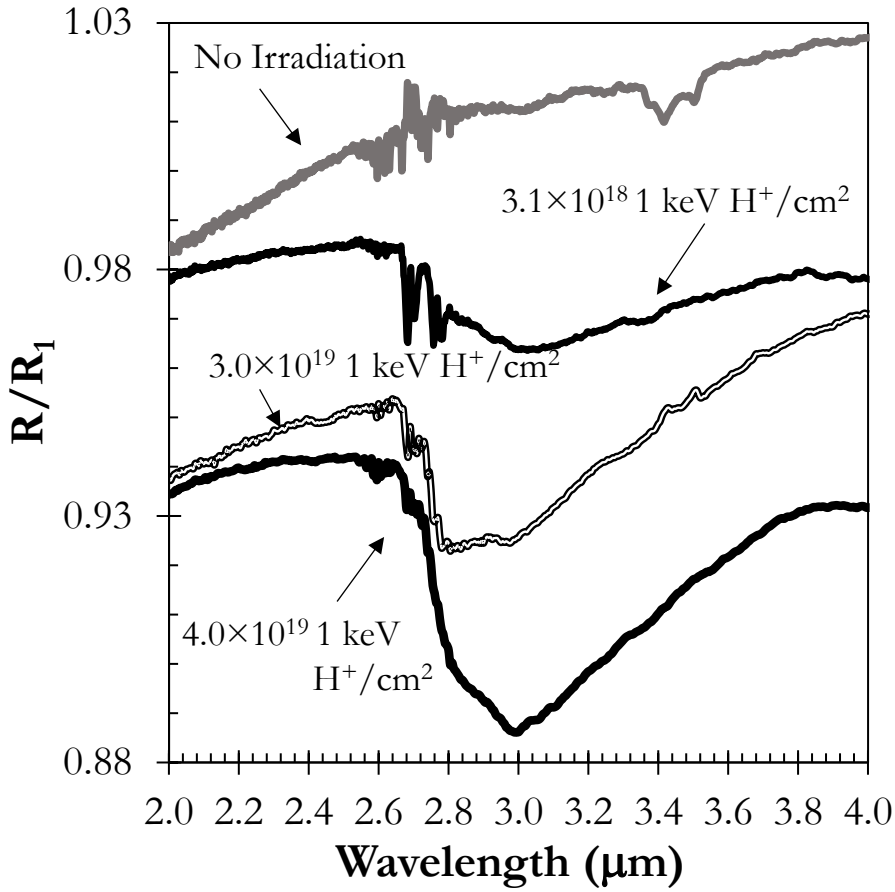

Figure 2. DRIFTS spectra of 78421 before and after proton irradiation. The spectra from top to bottom correspond to the unirradiated 78421 (back of sample) and after fluences of 0.31 ± 0.07, 3.0 ± 0.7, and 4.0 ± 1.0 × 10^{19} 1 keV H^+/cm^2. The sample irradiated to a fluence of 3.0 ± 0.7 × 10^{19} 1 keV H^+/cm^2 was from a follow-up experiment with an unused portion of the 78421 sample. The spectra have been vertically offset for clarity.

3.2 Proton Irradiation of Lunar Sample 78421

Figure 2 shows the DRIFTS spectra for the baked lunar sample at different fluences, where the reference, R_1, is the reflected intensity of the baked unirradiated 78421 sample. The most prominent change in Figure 2 is the development of a broad absorption ranging from 2.67 – 3.5 μm that deepens with increasing proton fluence and is centered at 3.0 μm. Like that of the fused silica sample, the reflectance spectrum of the unirradiated side of the sample was taken at end of the irradiation experiments and shows no OH band. However, there is a slight increase in organics between 3.3 to 3.6 μm, which could simply be due to a small difference in adsorbed organics present on the back of the sample.

The second curve from the top is the spectrum after irradiation to a total fluence of 3.1 ± 0.7 × 10^{18} ions/cm^2. Note that a broad feature develops that is centered at 3.0 μm. This broad 3.0 μm band continues to increase with a total proton fluence of 4.0 ± 1.0 × 10^{19} ions/cm^2 (bottom curve). Note that the third curve from the top is from a different irradiation experiment than the other three spectra in the figure. This follow-up experiment substantiated the proton-induced hydroxylation growth and peak position using an intermediate proton fluence of 3.0 ± 0.7 × 10^{19} ions/cm^2.

In Figure 3, we have replotted the Figure 2 spectra with an extended wavelength range. Due to the overlap of the OH stretch and the H_2O stretch near 3 μm, a useful diagnostic signature for water in a sample is the 6.1 μm bending mode for water [*Falk*, 1984; *McIntosh et al.*, 2017; *L Starukhina*, 2001]. In spectrum A of Figure 3, the reflectance spectrum of liquid water has been replotted from [*Hale and Querry*, 1973]. The relative depth of two bands of water at the 2.9 μm (a superposition of the ($\nu_1\nu + {}_3$) OH stretching mode), and the 6.1 μm H_2O bending mode (ν_2) is ~3:1. The lack of a 6.1 μm adsorption band in the proton-irradiated 78421 sample indicates that any adsorbed terrestrial H_2O is below the detection limit and does not contribute significantly to the broad 3 μm OH band observed after proton irradiation. An implication to the lack of a 6.1 μm is that proton irradiation alone does not form adsorbed water.

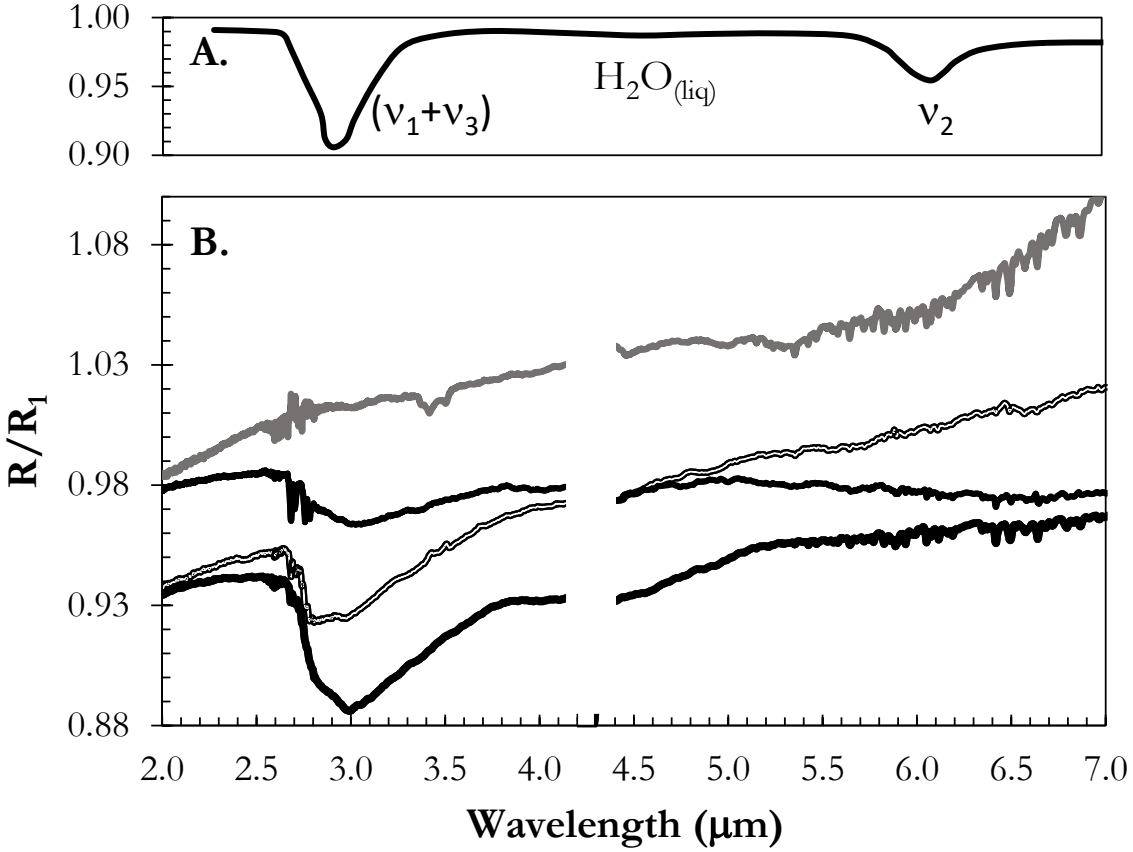

Figure 3. A. Reflectance spectrum [*Hale and Querry*, 1973] showing the ratio of ($\nu_1 + \nu_3$) versus ν_2 for adsorbed (multilayer) water and B. the DRIFTS spectra of 78421 from Figure 2 replotted with an expanded wavelength range. Spectra of the proton-irradiated 78421 are missing the ν_2 water band, and therefore internal water is not created during proton implantation nor is terrestrial adsorbed water contributing significantly to the broad 3μm OH band. For B., the region between 4.2 - 4.4 μm has been removed to eliminate the large ν_3 stretch band for $CO_{2(g)}$ present in the IR beam path.

3.3 Post-Irradiation Heating of 78421

Heating the 78421 sample after irradiation was motivated by the Moon's diurnal cycle where the temperature on the surface near the equator can reach near 400 K (127 °C) during noon [*Vasavada et al.*, 2012]. To perform the heating, we placed the irradiated sample into the sample holder located inside the FTIR compartment and heated at ~5 °C/min. The sample holder was held at 127 ± 2 °C for ~5 min, and then allowed to cool overnight to 25 °C. The heating was performed on the sample irradiated to a total proton fluence of $3.0 \pm 0.7 \times 10^{19}$ ions/cm^2, i.e., third curve from the top in Figure 2. The reflectance spectra of this sample before and after heating were converted to Kubelka-Munk (KM) units with the unit conversion function in the Nicolet iS50 software Omnic®, after which we removed the background continuum; the

resulting spectra are shown in Figure 4. Qualitatively the OH band after heating is very similar to the initial spectrum obtained after proton irradiation, although the band area appears to decrease by as much as 25% after heating to 400 K hydroxyl/hydrogen diffusion out of the sample could explain the spectral change and the decrease in band area (i.e., OH concentration) and might be attributed to recombinative desorption [*Jones et al.*, 2018].

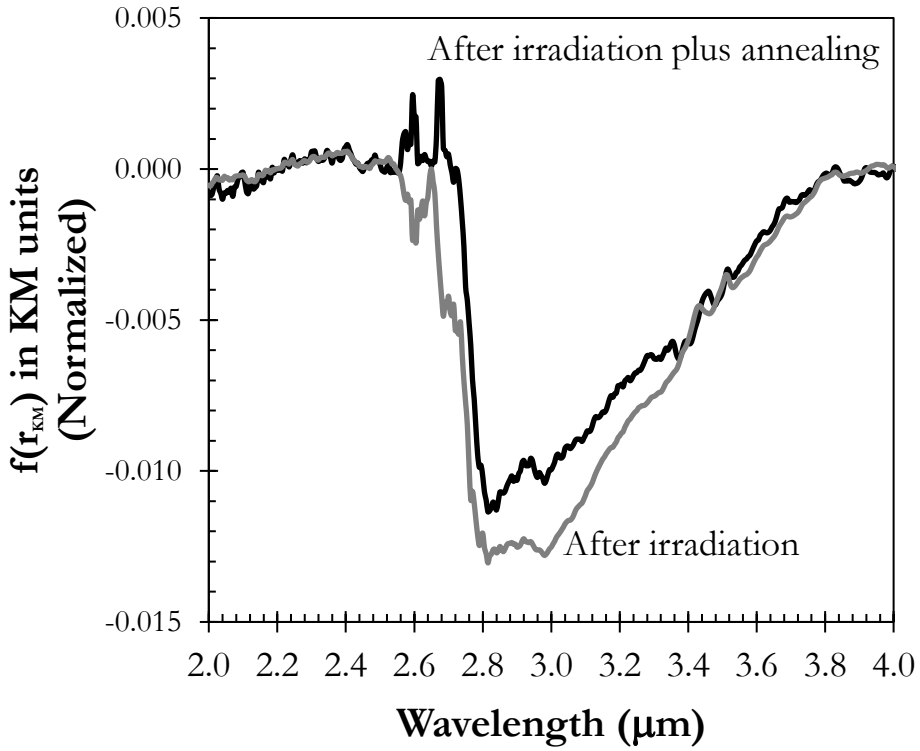

Figure 4. DRIFTS spectra of irradiated 78241 before and after heating to 400 K. Both measurements were taken at room temperature (~300 K). In both cases, the continuum has been removed using a non-linear baseline fit after converting the spectra to KM units.

4. Discussion

4.1 Comparison to Previous Proton Irradiation Study with Lunar Soils

In Figure 5, we compare our results to previous irradiation studies on Apollo 16 highlands (62241) and Apollo 17 mare (70051) regolith samples [*Ichimura et al.*, 2012]. The lunar samples in the Ichimura study were pre-heated in vacuum to remove any adsorbed telluric water. The main difference for the sample preparation is that for Ichimura et al. 2012, the samples were pre-heated to 500°C for 4 hours, and our 78421 sample was heated to 900°C for 4 hours. One striking result is the broadening of the OH band shapes of these dissimilar Apollo samples. Ichimura states the lack of a sharp OH feature is indicative of an amorphous material

and the OH band is inhomogeneously broadened. However, the OH band for our "amorphous" fused silica sample is still relatively sharp. Therefore, the heterogenous nature of the lunar samples may play a more important role for broadening the OH band due to the relationship of the OH vibrational energy with respect to the chemical environment [*Dyar et al.*, 2010]. Only seven minerals are found in greater than 1% abundance on the Moon: pyroxene (Ca, Fe^{2+}, Mg)SiO_3, plagioclase feldspar (Ca, Na)(Al, Si)$_4O_8$, ilmenite $Fe^{2+}TiO_3$, olivine (Mg, Fe^{2+})$_2SiO_4$, pyroxferroite $CaFe^{2+}{}_6(SiO_3)_7$, cristobalite SiO_2, and tridymite SiO_2 (Heiken et al. 1991). Of these minerals, only one (ilmenite) does not contain the structural silicon tetrahedral backbone. The lunar samples represent the topmost soils or lunar regolith, and have all experienced space weathering and have defects and inclusions of incompatible mineral type [*Lucey et al.*, 2006]. Nonetheless, in Figure 5 there are differences in these spectra regarding both band depth and position yet given that we see both parameters appear to vary between our two samples (see Figure's 1 and 2), more experiments are needed to determine whether or not these differences are significant. McCord et al. (2011) reports that the M^3 had two distinct IR absorptions, one at 2.8 μm and the other at 3.0 μm. If the inhomogeneous broadening of the OH band is due to a distribution of vibrational frequencies in various local environments and the population at each vibrational ensemble changes under different levels of proton irradiation, then the presented spectra of silica and 78421 seem to agree with McCord's two absorption bands. We may have observed two OH absorption bands in 78421. However, additional laboratory IR data is needed to more confidently determine whether these two absorptions are present in proton irradiated samples, and possibly how these two bands are influenced by fluence, temperature, or regolith mineralogy or maturity.

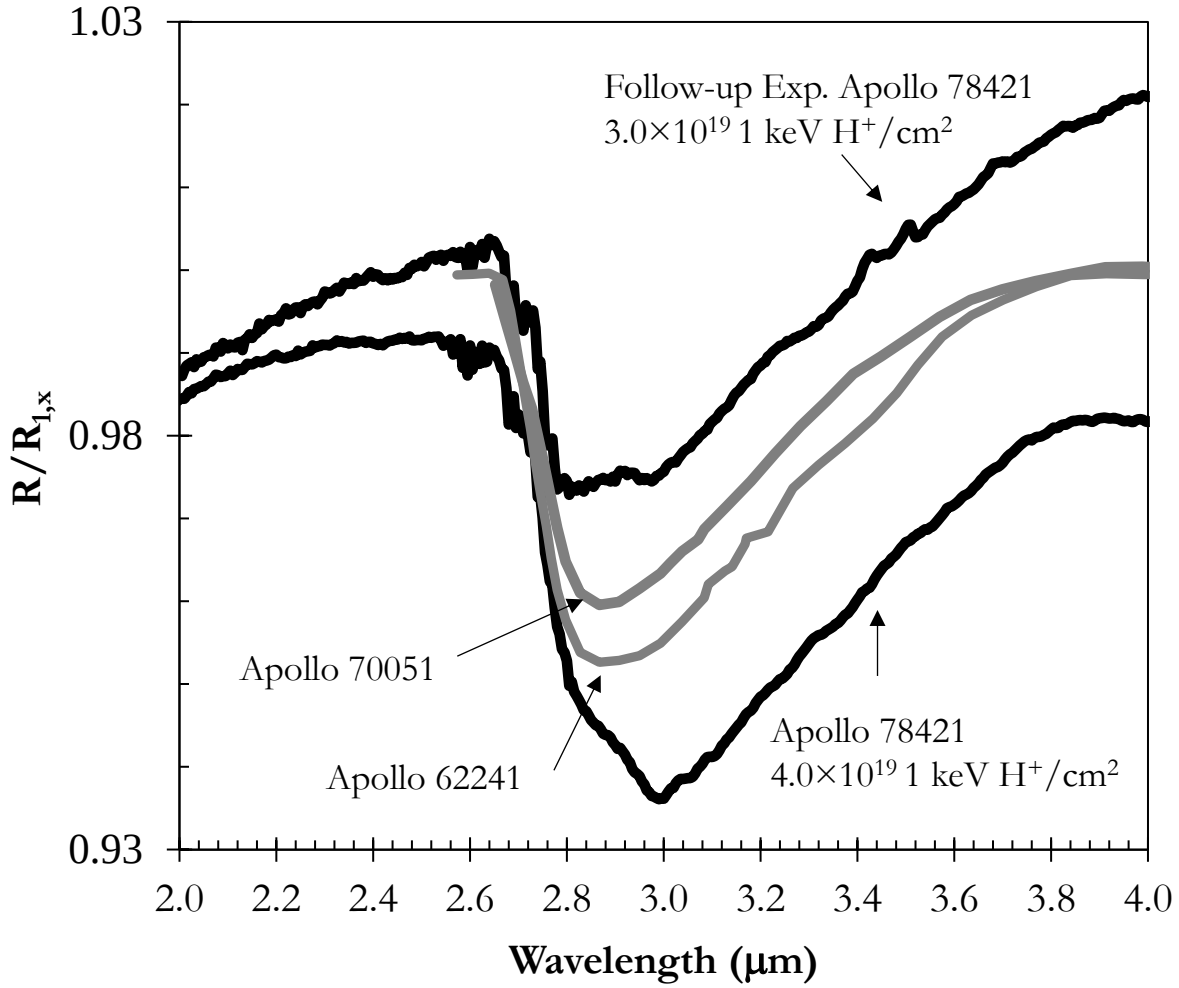

Figure 5. A comparison of proton-induced hydroxylation band shape from this study with the spectra of Ichimura et al. 2012. The black-line spectra are for 78421 from this study with a total proton fluence of $3.0 \pm 0.7 \times 10^{19}$ 1 keV H^+/cm^2 and $4.0 \pm 1.0 \times 10^{19}$ 1 keV H^+/cm^2. The grey spectra are from an Apollo 16 highlands sample 62241 and an Apollo 17 mare sample 70051 that have undergone similar proton irradiation.

4.2 Quantitative Results of Proton Induced Hydroxylation

Quantitative analyses by the DRIFTS method are complicated because from a theoretical standpoint there is no linear relationship between band intensity and concentration (as valid in transmission). However, if the reflectance spectrum is converted to Kubelka-Munk (KM) units, then the relationship of the spectral intensity to sample concentration is linear [*Kortum*, 1969; *Kubelka and Munk*, 1931]. The KM transform, $f(r_{KM})$, of the IR absorption band is approximately proportional to the absorption coefficient, and therefore is approximately proportional to the concentration of molecules creating the absorption feature. KM theory provides a linear relationship if the sample thickness is much greater than the IR penetration depth, which we

assume here, as the sample pellet thickness is ~2 mm and the IR beam is focused onto the sample surface. The linear relationship in KM units also assumes the absorber is highly dilute, and the scattering coefficient is constant. The former seems reasonable if one considers the entire volume probed by the IR light, although we expect that the OH will be more highly concentrated over the ion penetration depth. For our experiments, 78421 is a collection of compressed grains with an initial average size of 51 μm [*Graf*, 1993]. The scattering coefficient is a function of the particle size and packing. The particle size was likely unchanged due to post-irradiation heating. However, the packing density might have changed slightly during heating because of the aluminum ring sample holder (or the 78421 sample) thermally expanding and contracting. The outcomes of two different packing parameters are that an increase in packing results in an increase in absorbers, and therefore an increase in the band intensity, or vice-versa. If we assume that during post-irradiation heating the concentration of OH should not increase, the KM theory is an upper limit of OH removal after heating. For KM analysis, the two-stream solution of the radiative-transfer equation of an inhomogeneous sample is condensed into a single parameter, the scattering coefficient (*s*) [*Hapke*, 2012]. The KM remission function (r_{KM}) is:

$$r_{KM} = 1 + \frac{k}{s} - \sqrt{\frac{k}{s}\left(2 + \frac{k}{s}\right)} \qquad (1)$$

where *k* is the absorption coefficient. This equation can be solved for *k/s* which is the KM transform:

$$\frac{k}{s} = f(r_{KM}) = \frac{(1-r_{KM})^2}{2r_{KM}} = 2 * \frac{(1-r_{KM})^2}{4r_{KM}} = 2 * ESPAT \qquad (2)$$

where (ESPAT) is the Effective Single-Particle Absorption Thickness function for diffuse reflectance. From this expression, we can see that $f(r_{KM})$ is equal to 2 times the ESPAT function [*Hapke*, 2012]. The KM and ESPAT functions produce a linear relationship relative to the sample concentration. According to [*Hapke*, 2012] the KM theory misinterprets the physical nature of r_{KM}, however r_{KM} is still proportional to the true particle absorption coefficient due to fortuitous mathematics of the volume-averaged absorption efficiency and the scattering efficiency including diffraction.

Li and Milliken 2017 observed a linear trend between the ESPAT and water-equivalent OH% for a range of particle sizes. We have shown that it is not possible to determine the ratio between OH and H_2O near 3 μm, but since our spectral range extends past 6 μm, we conclude that our 3 μm band is primarily OH. For the following quantitative analysis, we equate our OH band feature from the hydroxylation from proton irradiation (water-equivalent OH%) and the water content (H_2O%) from the mid-ocean ridge basalt glass used by Li. For this analysis we convert our spectra to the ESPAT function and compare our data to the empirical data obtained by Li and Milliken 2017. For this analysis, the ESPAT values for our spectra were obtained at λ = 2.74 μm for the fused silica sample and λ = 3.0 μm for 78421, corresponding to the maximum in the OH absorption band depth. Here we compute the ESPAT function with the continuum removed and find the water-equivalent OH% from the Li and Milliken Supp. Material 2017, Figure S1B. Since there is a distribution of particle sizes for both our samples, fused silica (<150 μm) and 78421 (average = 51 μm), we used the average water-equivalent OH% from the four available particle size fractions measured of 0-45, 32-53, 63-75, 106-125 μm. The water-equivalent OH% from the ESPAT function analysis is presented in Table 1 for our irradiated

samples. We can then use the average weight percent OH to compute the effective column density of H bonded as OH (ρ_H) from the following equation from [*S Li*, 2016]:

$$water\text{-}equivalent\ OH\% = \frac{(\frac{P*\rho_H}{2*D})*N_A^{-1}*MW_{H_2O}}{\rho_{bulk}} \quad (3)$$

where P is the fraction of hydrogen bonded to oxygen, and in our case is 100%, because we are computing only hydroxyls measured from the 2.74 μm and 3.0 μm band depth analysis. D is the penetration depth for solar wind protons (~20 nm [Zeigler 2013]), N_A is Avogadro's number, MW_{H2O} is 18.0 g/mol for water, ρ_{bulk} is the bulk density, which is 2.2 g/mol for the fused silica and 1.8 g/mol for sample 78421 [*Mitchell et al.*, 1972], and the factor of 2 is to account for two hydrogen atoms in H_2O. From these data, we can also determine the conversion ratio for solar wind type ions to hydroxyl bond formation, (H_{ion}/OH_s) as presented in the last column in Table 1.

Table 1. Calculated column densities and conversion ratios for solar wind protons to water-equivalent OH based on the linear ESPAT function relationship from Li and Milliken 2017.

Sample	H^+ Fluence (1 keV H^+ /cm^2)[a]	ESPAT value[b]	Average OH%[c]	Column Density ρ_{OH} (OH/cm^2)	Conversion Ratio (H_{ion}/OH_s)[d]
Fused Silica	$7.8 \pm 1.8 \times 10^{18}$	8.0×10^{-5}	0.00007	2.0×10^{12}	$3.8 \pm 0.9 \times 10^{7}$
	$2.5 \pm 0.6 \times 10^{19}$	1.1×10^{-3}	0.00102	3.0×10^{13}	$8.3 \pm 2.0 \times 10^{6}$
Apollo 17 Sample 78421	$3.0 \pm 0.7 \times 10^{18}$	3.2×10^{-4}	0.00029	7.0×10^{12}	$4.3 \pm 1.0 \times 10^{6}$
	$3.0 \pm 0.7 \times 10^{19}$	9.5×10^{-4}	0.00088	2.1×10^{13}	$1.4 \pm 0.3 \times 10^{7}$
	$4.0 \pm 1.0 \times 10^{19}$	2.7×10^{-3}	0.00246	5.9×10^{13}	$6.8 \pm 1.7 \times 10^{6}$

a. Error was calculated from variation in the H_2^+ beam current.
b. ESPAT value was derived from the KM transformation at the maximum absorption depth in the DRIFTS spectra at λ = 2.74 μm for the fused silica, and λ = 3.0 μm for 78421.
c. Four size fractions (0-45, 32-53, 63-75, 106-125 μm) were extrapolated from Li and Milliken Supp. Material 2017, Fig. S1B.
d. The error was propagated from the variation in H_2^+ beam current.

We note that for our calculations, we used a solar wind proton penetration depth of 20 nm to be consistent with Transport of Ion in Matter (TRIM) calculations [*Ziegler*, 2013], instead of the 200 nm given in Li and Milliken [2016]. However, even though our ion beam was essentially monoenergetic, our previous simulations have shown that the penetration depth can be much deeper than 20 nm if other processes are considered [*Farrell et al.*, 2016; *Mattern et al.*, 1976]. The diffusion rate described by the Farrell et al. 2017 model, suggest that the hydroxyls will diffuse away from the near surface up to 100 nm on the timescale that the irradiation is performed, and possibly deeper. Local thermal spikes during proton implantation can also result in deeper penetration depth, which is not modeled within the TRIM code [*Tucker et al.*, 2005]. The depth profile is important because it directly relates to our computed conversion ratio, where if the penetration depth of 200 nm is chosen, as in Li and Milliken [2016], the H_{ion}/OH_s ratio decreases by an order of magnitude, meaning that 10 times less hydrogen is needed to form OH_s.

5 Conclusions

Our laboratory results show that the crushed fused silica needs to be relatively *hydroxyl free* to be able to observe an increase in the proton induced hydroxylation band at 2.74 μm using DRIFTS, which we accomplished by initially annealing our sample to 900 °C in vacuum. Subsequent induced hydroxylation experiments on 78421 show that its OH band is downshifted and much broader than the fused silica sample.

The OH band was slightly shifted to longer wavelengths when 78421 was heated to 400 K. Our analysis of the ESPAT value shows that the OH concentration due to heating to 400 K is up to 25% reduced. This is an upper limit due to the unknown extent of the change in the packing parameter after the thermal expansion and contraction of the sample and sample holder. The thermal effects are consistent with the diffusion of hydrogen in and/or out of lunar sample 78421.

Both the fused silica sample and 78421 sample were prepared under identical conditions regarding the annealing and compression into a pellet followed by proton irradiation. However, the space weathered 78421 OH band is much broader than of the fused silica powder. The broadening may be due to the heterogeneous nature of the space weathered 78421 sample.

Due to the inhomogeneous broadening of the OH band, the OH band easily encompasses the molecular water 2.9 μm OH stretching mode. The OH band for the highest fluence experiment is centered at 3.0 μm with a FWHM from 2.75-3.45 μm but ranges from 2.65 to 3.90 μm. The absence of a molecular water bending mode at 6.1 μm indicates that the broad OH band is not significantly affected by adsorbed terrestrial water. One interesting observation of these results is that the proton beam is also not creating the 6.1 μm feature and implies that solar wind protons do not directly produce measurable amounts of water.

By comparing different lunar samples that have undergone proton irradiation (Figure 5), we find that each sample spectrum exhibits a broad absorption band, even though there are small differences in both band depth and position. At this point, we cannot comment whether any differences are significant because we also observed that these parameters vary between our own samples, as well as with irradiation fluence (see Figure 2). New observations from the SOFIA observatory have indicated that 6.1 μm emission band is present at high lunar latitudes [*Honniball et al.*, 2020], suggesting that the lunar feature near 3 μm, in that region as well as possibly others, may be a combination of implanted OH and some form of water.

Finally, M^3 observations as described by McCord et al, 2011 found two distinct absorptions features, one narrow feature at 2.8 μm and one broader 3 μm feature. [*Bandfield et al.*, 2018] reported the widespread distribution of the two features. Our spectral data also shows a sharp peak at 2.74 μm for fused silica and a broad 3 μm feature for our lunar sample 78421, which may also contain a 2^{nd} feature near what was observed in the fused silica sample. Future higher resolution laboratory experiments will focus on determining whether there are two distinct bands in our irradiated lunar samples, which if confirmed, would suggest that both features observed with M^3 could be produced by solar wind implantation.

Acknowledgments, Samples, and Data

The authors would like to acknowledge SSERVI for DREAM2 Award #13-SSERVI13-0005 funding support. Special thanks to CAPTEM for the lunar sample loan agreement #17415. The authors would also like to thank the NASA Radiation Effects Facility staff. Our spectra data sets used to create Figures 1-4 are found at the Astomat.org. [*McLain,* 2021].

References

Bandfield, J. L., M. J. Poston, R. L. Klima, and C. S. Edwards (2018), Widespread distribution of OH/H2O on the lunar surface inferred from spectral data, *Nature Geoscience*, *11*(3), 173-+, doi:10.1038/s41561-018-0065-0.

Benna, M., D. Hurley, T. J. Stubbs, P. R. Mahaffy, and R. C. Elphic (2019), Lunar soil hydration constrained by exospheric water liberated by meteoroid impact, *Nature Geoscience*, *12*, 333-338.

Burke, D. J., C. A. Dukes, J. H. Kim, J. Shi, M. Fama, and R. A. Baragiola (2011), Solar wind contribution to surficial lunar water: Laboratory investigations, *Icarus*, *211*(2), 1082-1088, doi:10.1016/j.icarus.2010.11.007.

Clark, R. N. (2009), Detection of Adsorbed Water and Hydroxyl on the Moon, *Science*, *326*(5952), 562-564, doi:10.1126/science.1178105.

Colaprete, A., et al. (2010), Detection of Water in the LCROSS Ejecta Plume, *Science*, *330*(6003), 463-468, doi:10.1126/science.1186986.

Dyar, M. D., C. A. Hibbitts, and T. M. Orlando (2010), Mechanisms for incorporation of hydrogen in and on terrestrial planetary surfaces, *Icarus*, *208*(1), 425-437, doi:10.1016/j.icarus.2010.02.014.

Falk, M. (1984), THE FREQUENCY OF THE H-O-H BENDING FUNDAMENTAL IN SOLIDS AND LIQUIDS, *Spectroc. Acta Pt. A-Molec. Biomolec. Spectr.*, *40*(1), 43-48, doi:10.1016/0584-8539(84)80027-6.

Farrell, W. M., D. M. Hurley, V. J. Esposito, M. J. Loeffler, J. L. McLain, T. M. Orlando, R. L. Hudson, R. M. Killen, and M. I. Zimmerman (2015a), The Role of Crystal Defects in the Retention of Volatiles at Airless Bodies, paper presented at Space Weathering of Airless Bodies: An Integration of Remote Sensing Data, Laboratory Experiments and Sample Analysis Workshop, November 01, 2015.

Farrell, W. M., D. M. Hurley, V. J. Esposito, J. L. McLain, and M. I. Zimmerman (2017), The statistical mechanics of solar wind hydroxylation at the Moon, within lunar magnetic anomalies, and at Phobos, *J. Geophys. Res.-Planets*, *122*(1), 269-289, doi:10.1002/2016je005168.

Farrell, W. M., D. M. Hurley, and M. I. Zimmerman (2015b), Solar wind implantation into lunar regolith: Hydrogen retention in a surface with defects, *Icarus*, *255*, 116-126, doi:10.1016/j.icarus.2014.09.014.

Farrell, W. M., D. M. Hurley, and M. I. Zimmerman (2016), Solar wind implantation into lunar regolith: Hydrogen retention in a surface with defects (vol 255, pg 116, 2015), *Icarus*, *272*, 414-414, doi:10.1016/j.icarus.2016.03.016.

Fink, D., J. Krauser, D. Nagengast, T. A. Murphy, J. Erxmeier, L. Palmetshofer, D. Braunig, and A. Weidinger (1995), HYDROGEN IMPLANTATION AND DIFFUSION IN SILICON AND SILICON DIOXIDE, *Appl. Phys. A-Mater. Sci. Process.*, *61*(4), 381-388, doi:10.1007/bf01540112.

Graf, J. C. (1993), Lunar Soils Grain Size Catalog, *NASA Reference Pub. 1265*.

Hale, G. M., and M. R. Querry (1973), OPTICAL-CONSTANTS OF WATER IN 200-NM TO 200-MUM WAVELENGTH REGION, *Applied Optics*, *12*(3), 555-563, doi:10.1364/ao.12.000555.

Hapke, B. (2012), *Theory of Reflectance and Emittance Spectroscopy. pp. 318-321.*, Cambridge University Press.

Honniball, C. I., P. G. Lucey, S. Li, S. Shenoy, T. M. Orlando, C. A. Hibbitts, D. M. Hurley, and W. M. Farrell (2020), Molecular water detected on the sunlit Moon by SOFIA, *Nature Astronomy*, doi:10.1038/s41550-020-01222-x.

Hurley, D. M., et al. (2017), Contributions of solar wind and micrometeoroids to molecular hydrogen in the lunar exosphere, *Icarus*, *283*, 31-37, doi:10.1016/j.icarus.2016.04.019.
Ichimura, A. S., A. P. Zent, R. C. Quinn, M. R. Sanchez, and L. A. Taylor (2012), Hydroxyl (OH) production on airless planetary bodies: Evidence from H+/D+ ion-beam experiments, *Earth Planet. Sci. Lett.*, *345*, 90-94, doi:10.1016/j.epsl.2012.06.027.
Jones, B. M., A. Aleksandrov, K. Hibbitts, M. D. Dyar, and T. M. Orlando (2018), Solar Wind-Induced Water Cycle on the Moon, *Geophys. Res. Lett.*, *45*(20), 10959-10967, doi:10.1029/2018gl080008.
Kortum, G. (1969), *Reflectance Spectroscopy*, Springer, New York.
Kubelka, P., and F. Munk (1931), Ein Beitrag zurOptik der Farberntricke, *Z. Techn. Physik*, *12*, 593-601.
Li, and R. E. Milliken (2017), Water on the surface of the Moon as seen by the Moon Mineralogy Mapper: Distribution, abundance, and origins, *Sci. Adv.*, *3*(9), 11, doi:10.1126/sciadv.1701471.
Li, S. (2016), Water on the Lunar Surface as Seen by the Moon Mineralogy Mapper: Distribution, Abundance, and Origins, Brown University, Providence, Rhode Island.
Lucey, P., et al. (2006), Understanding the lunar surface and space-moon interactions, in *New Views of the Moon*, edited by B. L. Jolliff and M. A. Wieczorek, pp. 83-+, doi:10.2138/rmg.2006.60.2.
Mattern, P. L., G. J. Thomas, and W. Bauer (1976), Hydrogen and Helium Implantation in Vitreous Silica, *Journal of Vacuum Science & Technology*, *13*(1), 430-436, doi:10.1116/1.568938.
McCord, T. B., L. A. Taylor, J. P. Combe, G. Kramer, C. M. Pieters, J. M. Sunshine, and R. N. Clark (2011), Sources and physical processes responsible for OH/H(2)O in the lunar soil as revealed by the Moon Mineralogy Mapper (M(3)), *J. Geophys. Res.-Planets*, *116*, doi:E00g05 10.1029/2010je003711.
McIntosh, I. M., A. R. L. Nichols, K. Tani, and E. W. Llewellin (2017), Accounting for the species-dependence of the 3500 cm(-1) H2Ot infrared molar absorptivity coefficient: Implications for hydrated volcanic glasses, *Am. Miner.*, *102*(8), 1677-1689, doi:10.2138/am-2017-5952CCBY.
McLain, J. L. (2021), Proton Irradiation Experiments: DRIFTS Spectra of Apollo 17 soil 78421 and a Fused Silica Reference, *Version 1.0. Interdisciplinary Earth Data Alliance (IEDA).* , doi:https://doi.org/10.26022/IEDA/111825.
Mitchell, J. K., R. F. Scott, L. G. Bromwell, W. D. Carrier, and N. C. Costes (1972), SOIL MECHANICAL PROPERTIES AT APOLLO-14 SITE, *Journal of Geophysical Research*, *77*(29), 5641-&, doi:10.1029/JB077i029p05641.
Morris, R. V. (1978), The surface exposure (maturity) of lunar soils: Some concepts and Is/FeO compilation, *Proc. 9th Lunar Sci. Conf.*
Pieters, C. M., et al. (2009), Character and Spatial Distribution of OH/H2O on the Surface of the Moon Seen by M-3 on Chandrayaan-1, *Science*, *326*(5952), 568-572, doi:10.1126/science.1178658.
Schaible, M. J., and R. A. Baragiola (2014), Hydrogen implantation in silicates: The role of solar wind in SiOH bond formation on the surfaces of airless bodies in space, *J. Geophys. Res.-Planets*, *119*(9), 2017-2028, doi:10.1002/2014je004650.

Starukhina, L. (2001), Water detection on atmosphereless celestial bodies: Alternative explanations of the observations, *J. Geophys. Res.-Planets*, *106*(E7), 14701-14710, doi:10.1029/2000je001307.
Starukhina, L. V. (2006), Polar regions of the moon as a potential repository of solar-wind-implanted gases, in *Moon and near-Earth Objects*, edited by P. Ehrenfreund, B. Foing and A. Cellino, pp. 50-58, Elsevier Science Bv, Amsterdam, doi:10.1016/j.asr.2005.04.033.
Stern, S. A., J. C. Cook, J. Chaufray, P. D. Feldman, G. R. Gladstone, and K. D. Retherford (2013), Lunar atmospheric H2 detections by the LAMP UV spectrograph on the Lunar Reconnaissance Orbiter, *Icarus*, *226*.
Sunshine, J. M., T. L. Farnham, L. M. Feaga, O. Groussin, F. Merlin, R. E. Milliken, and M. F. A'Hearn (2009), Temporal and Spatial Variability of Lunar Hydration As Observed by the Deep Impact Spacecraft, *Science*, *326*(5952), 565-568, doi:10.1126/science.1179788.
Tucker, O. J., W. M. Farrell, R. M. Killen, and D. M. Hurley (2019), Solar Wind Implantation Into the Lunar Regolith: Monte Carlo Simulations of H Retention in a Surface With Defects and the H-2 Exosphere, *J. Geophys. Res.-Planets*, *124*(2), 278-293, doi:10.1029/2018je005805.
Tucker, O. J., D. S. Ivanov, L. V. Zhigilei, R. E. Johnson, and E. M. Bringa (2005), Molecular dynamics simulation of sputtering from a cylindrical track: EAM versus pair potentials, *Nucl. Instrum. Methods Phys. Res. Sect. B-Beam Interact. Mater. Atoms*, *228*, 163-169, doi:10.1016/j.nimb.2004.10.040.
Vasavada, A. R., J. L. Bandfield, B. T. Greenhagen, P. O. Hayne, M. A. Siegler, J. P. Williams, and D. A. Paige (2012), Lunar equatorial surface temperatures and regolith properties from the Diviner Lunar Radiometer Experiment, *J. Geophys. Res.-Planets*, *117*, doi:10.1029/2011je003987.
Wieser, M., S. Barabash, Y. Futaana, M. Holmstrom, A. Bhardwaj, R. Sridharan, M. B. Dhanya, P. Wurz, A. Schaufelberger, and K. Asamura (2009), Extremely high reflection of solar wind protons as neutral hydrogen atoms from regolith in space, *Planetary and Space Science*, *57*(14-15), 2132-2134, doi:10.1016/j.pss.2009.09.012.
Wieser, M., P. Wurz, K. Bruning, and W. Heiland (2002), Scattering of atoms and molecules off a magnesium oxide surface, *Nuclear Instruments & Methods in Physics Research Section B-Beam Interactions with Materials and Atoms*, *192*(4), 370-380, doi:10.1016/s0168-583x(02)00486-x.
Zeller, E. J., L. B. Ronca, and P. W. Levy (1966), Proton-Induced Hydroxyl Formation on Lunar Surface, *Journal of Geophysical Research*, *71*(20), 4855-&.
Zhuravlev, L. T. (2000), The surface chemistry of amorphous silica. Zhuravlev model, *Colloid Surf. A-Physicochem. Eng. Asp.*, *173*(1-3), 1-38, doi:10.1016/s0927-7757(00)00556-2.
Ziegler, J. F. (2013), PARTICLE INTERACTIONS WITH MATTER, edited.